RESEARCH ARTICLE

ADVANCED
MATERIALS
INTERFACES
Open Access

www.advmatinterfaces.de

Acoustic Wave Engineering of Lamb Wave Resonators with 2D van der Waals Floating Electrode

Seok Hyun Yoon, Cheul Hyun Yoon, and Byoung Don Kong*

Lamb wave resonators with 2D van der Waals floating electrodes are investigated to overcome the intrinsic RF performance limitations of conventional floating electrodes. By utilizing graphene as the floating electrode and hexagonal boron nitride as an acoustic mirror, the resonators achieve enhanced resonance frequency, electromechanical properties, and energy confinement compared to the conventional Pt floating electrodes. Finite element method simulations show that the graphene floating electrode significantly enhances S0 mode resonance frequency and electromechanical coupling coefficient. Incorporating the hexagonal boron nitride interlayer further improves the Q-factor by 1.4 times, effectively confining acoustic energy within the AlN layer. The newly implemented 2D heterostructure demonstrates resonance frequencies above 7 GHz, a maximum figure of merit of 1152, and outstanding temperature stability with a temperature coefficient of frequency of −29.02 ppm/°C. This research demonstrates the potential for developing high-performance Lamb wave resonator operating in the cm-Wave band (7-15 GHz). Additionally, the 2D heterostructure provides a versatile platform adaptable to various acoustic wave devices.

1. Introduction

The rapid advancement of wireless communication technology, alongside the proliferation of data-intensive technologies such as the Internet of Things (IoT), artificial intelligence (AI), autonomous driving, and large-scale data processing, has led to increasing congestion in frequency bands.[1] This trend intensifies the demand for high-performance acoustic wave resonator technology, which is crucial for radio frequency front-ends (RFFEs) in advanced wireless communication systems.[2]

The emerging 6G wireless communications standard is particularly focused on the cm-Wave bands (7–15 GHz), including the X-band (7–12 GHz). This upper mid-band spectrum, known

S. H. Yoon, C. H. Yoon, B. D. Kong
Department of Electrical Engineering
Pohang University of Science and Technology (POSTECH)
Pohang 37673, Republic of Korea
E-mail: bdkong@postech.ac.kr

as Frequency Range 3 (FR3), is positioned between FR1 (sub-6G, 410 MHz-7.125 GHz) and FR2 (mm-Wave, 24.25–71 GHz).[3] The FR3 offers an optimal balance between high capacity and good coverage, with the 7.1–8.4 GHz band identified as a prime candidate for 6G services.[4]

Aluminum nitride (AlN)-based Lamb wave resonators (LWRs) have emerged as promising candidates for radio frequency (RF) applications.[5–8] LWRs combine the advantages of both surface acoustic wave (SAW) and bulk acoustic wave (BAW) devices, offering frequency tunability through SAW lithography technology and the high Q-factor of BAW devices.[9] This unique characteristic allows LWRs to achieve high RF performances while supporting multiple resonance frequencies (f_r) on a single chip. Among various LWR structures, those employing floating electrodes (FEs) stand out for their high electromechanical coupling coefficient (k^2), high-quality factors (Q-factors), and CMOS compatibility.[10]

2D materials, including graphene, hexagonal boron nitride (hBN), and transition metal dichalcogenides (TMDCs), have opened new opportunities for nanomechanical resonators.[11,12] In particular, one promising approach to enhance LWR performance involves using graphene as electrodes.[13–15] Graphene's atomically thin, ultralow mass density (ρ) structure—combined with its high Young's modulus (E)—eliminates mass loading while enforcing a near-zero interfacial strain via weak van der Waals interaction, thereby minimizing mechanical damping, increasing acoustic wave velocity ($\sqrt{E/\rho}$), and significantly increasing f_r, making it an ideal electrode for high-frequency applications. However, it is worth noting that as devices operate at high f_r, maintaining a high k^2 and Q-factor remain increasingly challenging due to various loss mechanisms, including the quality of graphene itself.[16–20]

Since the lamb waves are guided acoustic waves that result from superposition of longitudinal and transverse waves,[21] the performance of LWR devices is significantly influenced by acoustic impedance (Z) at material interfaces. It plays a crucial role in determining how acoustic waves propagate and interact at boundaries between different materials.[10,15] Mismatches in Z between layers affect device performance, particularly the Q-factor, requiring careful interface engineering to optimize energy confinement and coupling while minimizing losses.

ADVANCED
SCIENCE NEWS

www.advancedsciencenews.com

ADVANCED
MATERIALS
INTERFACES
Open Access
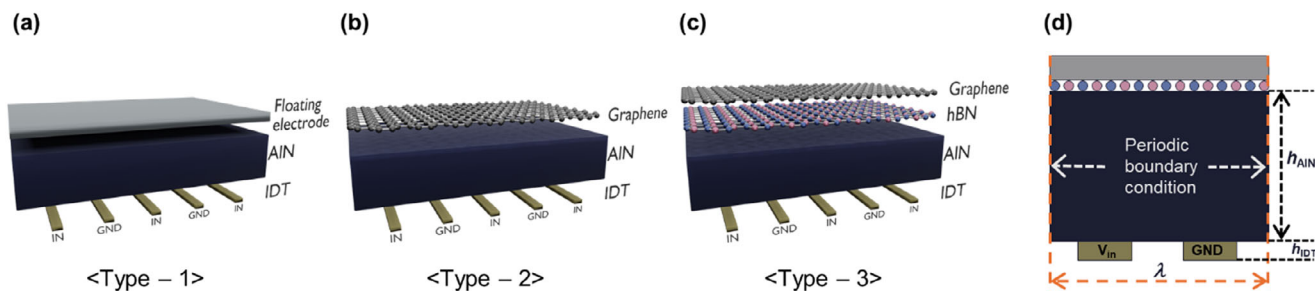
www.advmatinterfaces.de

Figure 1. Schematic illustrations of the three AlN-based FE-LWR structures and the unit cell model. a) Type-1 (IDT/AlN/FE), b) Type-2 (IDT/AlN/graphene FE), and c) Type-3 (IDT/hBN/AlN/graphene FE) LWRs. d) 2D unit cell model used for FEM simulations to analyze the frequency response. Periodic boundary conditions were applied to the left and right sides, and a sinusoidal signal was used for excitation with $\lambda = 1.2\ \mu m$.

Furthermore, temperature stability, quantified by the temperature coefficient of frequency (TCF), is crucial for device reliability.[22] Given these constraints, achieving excellent RF characteristics at high f_r remains a significant challenge in the field of acoustic wave devices.

In this study, we explore the enhancement of LWR RF performance through the integration of a 2D van der Waals heterostructure composed of hBN and graphene. Among 2D materials, hBN stands out for its highly anisotropic characteristics and exceptional piezoelectric properties, which are expected to further improve device performance.[23] The hBN/graphene heterostructure was employed to induce acoustic wave reflections at the interface, thereby confining acoustic energy and mitigating interfacial acoustic losses arising from acoustic impedance mismatch. The RF performance of hBN/graphene-based LWR devices was systematically compared to that of conventional Pt FE and graphene FE LWRs, with variations in AlN thickness. This work is based on theoretical and computational analysis, intended to guide and inform subsequent experimental investigations. Additionally, the TCF of the hBN/graphene heterostructure was analyzed, with particular emphasis on frequency stability under high-frequency operating conditions.[24]

2. Device Modeling and Simulation

Three types of AlN-based FE-LWR structures were investigated: Interdigital transducer (IDT)/AlN/FE (Type-1), IDT/AlN/graphene FE (Type-2), and IDT/hBN/AlN/graphene FE (Type-3), as shown in **Figure** 1a–c. Typically, Pt is used as a FE due to its stability and high Z. However, its high mass density (ρ) limits both high-frequency performance and electromechanical coupling efficiency. For this reason, Pt was replaced with graphene in Type-2 LWR, utilizing its high E and low mass density to improve the f_r and k^2. Type-3 LWR integrates an hBN interlayer, which reflects acoustic waves to reduce the loss by the acoustic energy confinement effect.

To analyze the frequency response of these LWR structures, finite element method (FEM) simulations using a 2D unit cell model were adopted as illustrated in Figure 1d. Periodic boundary conditions were applied to the left and right sides of the model, and a sinusoidal signal was applied for excitation. RF characteristics were analyzed across the range of AlN normalized thicknesses (h_{AlN}/λ) from 0.1 to 1, with $\lambda = 1.2\ \mu m$. **Table** 1 summarizes the material constants for AlN and hBN, including

elastic (C), piezoelectric (e), dielectric tensors (ϵ), and tangential loss tangent (tanδ). In our analysis, the tanδ reflects both intrinsic material properties and contributions from the interface-related losses, providing a more practical device operation.[22,23,25] Given that the λ used in our simulation is several orders of magnitude larger than atomic-scale defects, the effects of local imperfections are expected to be statistically averaged out and are thus collectively included in the bulk acoustic loss modeled by tanδ, and do not significantly affect acoustic wave propagation. For Type-1 LWR, 50 nm of Pt was employed as the FE due to its high acoustic impedance and chemical stability, whereas the thicknesses of monolayer graphene and hBN were set 0.335 and 0.333 nm, respectively. Au was used for the IDTs with a $h_{Au}/\lambda = 0.02$ in all three cases, chosen for its low resistivity—a crucial factor for high-frequency operation.[26]

An inverted structure was studied in our simulations considering the feasibility. This design concept reverse the conventional stacking order of FE (bottom)-piezoelectric material-IDT (top). Yet, this design minimizes potential fabrication-related issues. In specific, during RF sputtering of AlN, graphene and hBN layers could potentially be damaged.[27]

Table 1. Material constants used in the simulations. These values are employed in the acoustic-electric simulations based on the stress-charge form of the piezoelectric constitutive equations.

	Symbol	AlN	hBN
Density [kg/m³]	ρ	3260	2180
Elastic constants [GPa]	C_{11}	345	928.78
	C_{12}	125	211.26
	C_{13}	120	2.57
	C_{33}	395	31.98
	C_{44}	118	17.83
	C_{66}	110	358.76
Piezoelectric constants [C/m²]	e_{15}	−0.48	2.68
	e_{31}	−0.58	2.68
	e_{33}	1.55	0.82
Relative permittivity	ϵ_{11}	8.0	6.61
	ϵ_{33}	9.5	3.76
Dielectric loss tangent	tanδ	0.003	6.5×10^{-6}
Refs.	–	[22]	[23, 25]

**ADVANCED
SCIENCE NEWS**

www.advancedsciencenews.com

**ADVANCED
MATERIALS
INTERFACES**
Open Access

www.advmatinterfaces.de

Table 2. Temperature coefficients of material constants used in the simulations. These values are utilized to investigate the temperature stability.

	Symbol	AlN	hBN	Graphene	Au
Thermal expansion coefficient [$\times 10^{-6}$/K]	α_{11}	5.3	−2.76	−8	14
	α_{33}	4.2	–	–	14
Refs.	–	[28]	[29]	[30]	[31]

The key RF performance indicators, k^2 and Q-factor, were calculated using the following equations:

$$k^2 = \frac{\pi}{2} \frac{f_r}{f_a} \tan\left(\frac{\pi}{2} \frac{f_a - f_r}{f_a} \right) \tag{1}$$

$$Q = \frac{f_r}{\Delta f_{3dB}} \tag{2}$$

where f_r and f_a are the resonance and anti-resonance frequency, respectively, and Δf_{3dB} is the 3 dB bandwidth.

To evaluate the thermal stability of the devices, the temperature-dependent material properties were incorporated as follows. The temperature dependence of the ρ and elastic tensor (C_{ij}) can be expressed as:

$$\rho(T) = \rho(T_0) \left[1 - \left(\alpha_{11} + \alpha_{22} + \alpha_{33} \right) \Delta T \right] \tag{3}$$

$$C_{ij} = C_{ij}(T_0) \left(1 + TC_{ij} \Delta T \right) \tag{4}$$

where T_0 is the reference temperature of the material constants, ΔT is the temperature change, α_{ij} are the linear thermal expansion coefficients along the x, y, and z-axis, and TC_{ij} are the temperature coefficients of elastic constants (TCEs).

By implementing these temperature functions for all relevant material properties, the simulation accurately describes how thermal expansion and stiffness variations in each constituent layer quantitatively contribute to the overall TCF. The TCF is defined as:

$$TCF = \frac{1}{f_r} \frac{\partial f}{\partial T} \tag{5}$$

which describes essentially how much the f_r changes by temperature variations. This approach enables a comprehensive analysis of how each material's thermal properties affect the device's f_r across a wide temperature range. The analysis was conducted over the range from –40 °C to 200 °C (step 20 °C) to thoroughly assess the thermal behavior of the devices. **Table 2** presents the temperature coefficients of material constants used in the simulations.[28–31]

The RF characteristics were extracted from the simulation results by analyzing the admittance curves and S-parameters to calculate the relevant parameters using established methods. Mesh optimization and convergence studies were performed to ensure the accuracy of our FEM simulations using COMSOL Multiphysics version 6.2 with AC/DC and structural mechanics modules. Material-specific loss factors to account for energy dissipation in each layer were incorporated into our simulation to ensure a more accurate description of device behaviors.

3. Results and Discussion

3.1. RF Performance Enhancement by Graphene Floating Electrodes

By adopting graphene as a field electrode (FE), the Type-2 LWR demonstrated marked improvements in RF performance compared to Type-1 LWRs. **Figure** 2a,b display the admittance curves for the A0 mode in Type-1 and Type-2 LWRs, respectively, as a function of normalized AlN thickness. As h_{AlN} increases, the resonance frequency (f_r) in both structures saturates below the 4 GHz band, with weak resonance peaks leading to reduced k^2 and Q-factor. In contrast, Figure 2c,d show that the S0 mode maintains a higher f_r and reveals stronger, more distinct resonance peaks than the A0 mode. These observations demonstrate the S0 mode's greater potential for RF performance enhancement, and therefore serve as the primary focus for the subsequent analysis.

The replacement of Pt FEs with graphene significantly enhances the fr of AlN-based LWRs, as demonstrated by the comparative analysis of Type-1 and Type-2 LWRs. **Figure** 2e presents a comparison of the S0 mode f_r in Type-1 and Type-2 LWRs. Notably, at $h_{AlN}/\lambda = 0.3$ (AlN thickness of 360 nm), Type-2 LWR achieved a maximum f_r of 7.3 GHz, ≈1.5 times higher than the maximum frequency of Type-1 LWR. The f_r can be attributed to graphene's high Young's modulus (≈1000 GPa) and virtually massless nature, as f_r proportional to $\sqrt{E_{eq}/\rho_{eq}}$. The equivalent parameters (x_{eq}) were calculated as the weighted average of each material's parameters over its thickness, as shown in the following equation:

$$x_{eq} = \frac{x_{FE} \cdot t_{FE} + x_{AlN} \cdot t_{AlN} + x_{IDT} \cdot t_{IDT}}{t_{FE} + t_{AlN} + t_{IDT}} \tag{6}$$

where x represent the parameters such as Young's modulus (E) and mass density (ρ) for the FE, AlN, and IDT, respectively, and t is their corresponding thickness.

The admittance curves and field distributions confirm that graphene's exceptional mechanical properties enable efficient acoustic energy confinement in thin AlN layers, facilitating high-frequency operation. Figure 2f shows the admittance curves for Type-1 and Type-2 LWRs at $h_{AlN}/\lambda = 0.3$, illustrating the increase in f_r. The displacement field and electric potential distributions of the S0 mode (Figure 2g) provide critical insights into the electromechanical coupling mechanisms governing wave propagation in graphene FE LWRs, aligning well with theoretical S0 mode characteristics. The displacement field illustrates the physical movement of particles in the material, while the electric potential distribution indicates charge distribution across the device, which is crucial for understanding the electromechanical coupling in acoustic wave devices.[32] This frequency increase is particularly pronounced for $h_{AlN}/\lambda < 0.5$, where acoustic energy can be effectively confined across the AlN thin film.

The k^2 also exhibited significant improvement with the graphene FE, as shown in **Figure** 3a. This enhancement can be attributed to graphene's high Z, and its low mass density. These properties synergistically improve the efficiency of energy conversion between electrical and mechanical domains. Despite the improvements in f_r and k^2, the Q-factor of Type-2 LWR did

e00502 (3 of 8)

ADVANCED
SCIENCE NEWS
www.advancedsciencenews.com

ADVANCED
MATERIALS
INTERFACES
Open Access
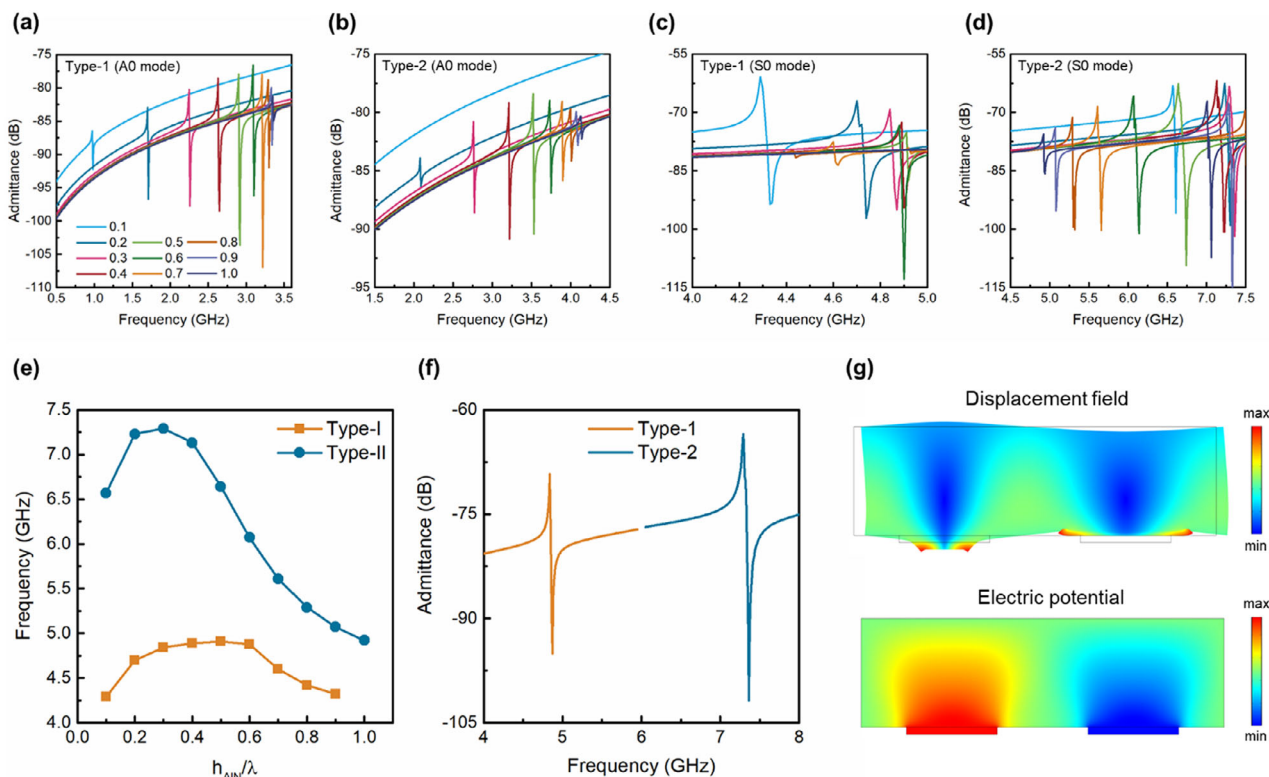www.advmatinterfaces.de

Figure 2. Comparison of frequency response between Type-1 and Type-2 LWRs. a,b) Admittance curves for the A0 mode in Type-1 and Type-2 LWRs, respectively, showing increasing f_r with h_{AlN}/λ from 0.1 to 1, which gradually saturates and weakens. c,d) Admittance curves for the S0 mode in Type-1 and Type-2 LWRs, respectively, demonstrating higher f_r and k^2 values compared to the A0 mode. e) f_r comparison of Type-1 and Type-2 LWRs across varying h_{AlN}/λ, showing a maximum fr of 7.3 GHz for Type-2 LWR at $h_{AlN}/\lambda = 0.3$ (AlN = 360 nm). f) Admittance curves for Type-1 and Type-2 LWRs at $h_{AlN}/\lambda = 0.3$, illustrating the significant increase in f_r for Type-2 LWR. g) Displacement field and electric potential distributions of the S0 mode in Type-2 LWR at $h_{AlN}/\lambda = 0.3$, showing alignment with S0 mode wave characteristics.

not show big improvement, mostly staying below 250. The Q-factor of Type-2 LWR even got lower than that of Type-1 LWR when h_{AlN}/λ was below 0.4, as illustrate in Figure 3b. For devices with thick h_{AlN} ($h_{AlN}/\lambda > 0.7$), the resonance feature was missing due to increased electrical resistance and energy loss from the thin IDTs. This appear as the missing data points in Figure 3b. The increased electrical resistance leads to higher motional resistance and weak electromechanical coupling. The Figure of Merits (FoMs) for these devices, the product of the k^2 and the Q-factor, serve as an comprehensive indicator of resonator performance
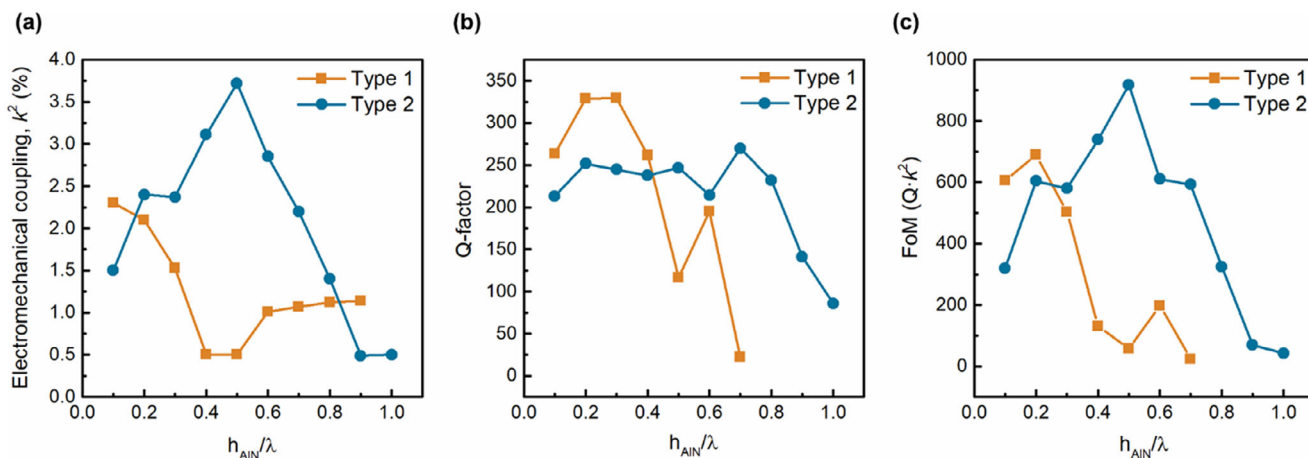

Figure 3. RF characteristics for Type-1 and Type-2 LWRs as a function of h_{AlN}/λ. a) shows results for k^2, showing significant improvement in k^2 for Type-2 LWR, b) for Q-factor, where the Type-2 LWR shows lower Q-factor compared to Type-1 LWR for $h_{AlN}/\lambda \leq 0.4$, and c) for FoM.

**ADVANCED
SCIENCE NEWS**

www.advancedsciencenews.com

**ADVANCED
MATERIALS
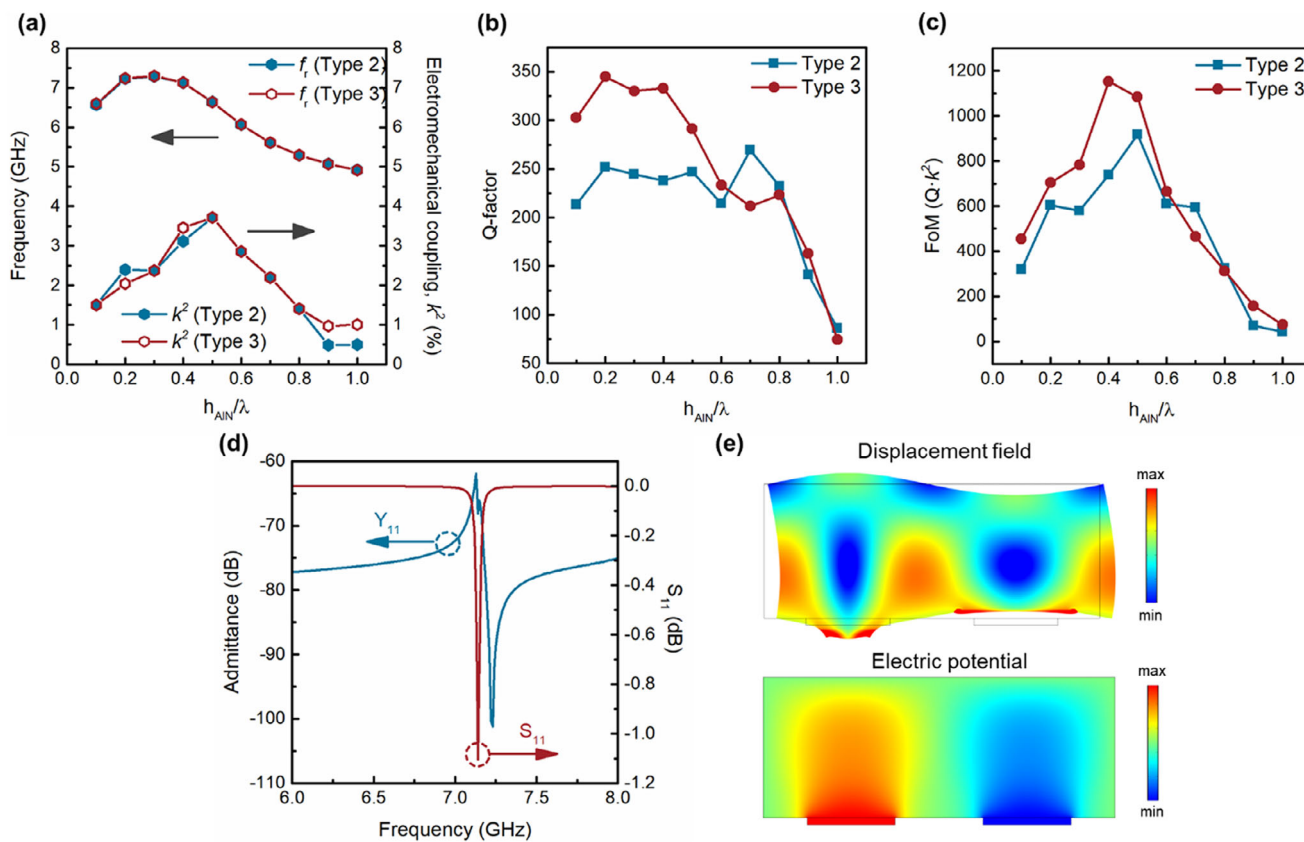INTERFACES**
Open Access

www.advmatinterfaces.de

Figure 4. Comparative analysis of RF performance metrics for Type-2 and Type-3 LWRs. a) shows results for S0 mode f_r and k^2 as a function of h_{AlN}/λ, showing nearly identical behavior, b) for Q-factor, where Type-3 LWR demonstrates a significant increase compared to Type-2 LWR for $h_{AlN}/\lambda \leq 0.5$, and c) for FoM, achieving a maximum value of 1152 at $h_{AlN}/\lambda = 0.4$ for Type-3 LWR. d) Admittance curve and S_{11} at $h_{AlN}/\lambda = 0.4$, demonstrating frequency response for Type-3 LWR. e) Displacement field and electric potential distributions for the S0 mode at $h_{AlN}/\lambda = 0.4$, illustrating how acoustic waves are confined and energy is distributed within the device structure.

by reflecting both energy storage efficiency and electromechanical energy conversion, are shown in Figure 3c.

While these findings demonstrate the potential of graphene FE-LWR devices by analyzing their RF characteristics as a function of AlN normalized thickness, the relatively low Q-factor, especially for thinner AlN layers, remains as a challenge that needs to be addressed for optimal device performance for 6G applications. In the following section, this approach to improve the Q-factor limitation is explored.

3.2. Acoustic Wave Engineering with hBN Heterointerfaces

3.2.1. Q-factor Enhancement with hBN Interlayer

The introduction of an hBN layer between AlN and graphene (Type-3 LWR) forms a graphene/hBN van der Waals heterostructure, which significantly enhances Q-factor while preserving the high f_r and k^2 of the graphene FE. This improvement directly addresses the critical requirements for frequency selectivity and signal stability in 6G upper mid-band applications. As shown in **Figure** 4a, f_r and k^2 of the S0 mode for Type-3 LWR are nearly identical to those of Type-2 LWR across the entire range of h_{AlN}/λ.

This similarity is attributed to the atomically thin and massless nature of hBN, which induces virtually no changes in the overall E_{eq} and ρ_{eq} of the device. Remarkably, the integration of the hBN interlayer results in a significant increase in Q-factor for $h_{AlN}/\lambda \leq 0.5$, as shown in Figure 4b. Type-3 LWR achieves a maximum Q-factor of 333 and a FoM of 1152 at $h_{AlN}/\lambda = 0.4$ (Figure 4c), representing a more than twofold improvement over Type-2 LWR. The admittance curve and S_{11} at this optimal point ($h_{AlN}/\lambda = 0.4$) are illustrated in Figure 4d, demonstrating well-defined resonance characteristics. The displacement field and electric potential distribution demonstrated in Figure 4e validate effective acoustic energy confinement within the AlN layer for the S0 mode. The S0 mode, which confines energy within the AlN bulk, benefits more from the heterostructure's acoustic confinement, whereas the A0 mode, with energy concentrated near the surface, is more affected by leakage; therefore, the S0 mode shows greater improvement.

3.2.2. Acoustic Wave Confinement Mechanism with hBN/Graphene Acoustic Mirror

The improvement in Q-factor in Type-3 LWR has turned out to originate from the acoustic impedance mismatch at the

**ADVANCED
SCIENCE NEWS**

www.advancedsciencenews.com

**ADVANCED
MATERIALS
INTERFACES**

www.advmatinterfaces.de

Table 3. Material properties of AlN, *h*BN, graphene, and Au used in analyzing the acoustic wave propagation and acoustic impedance mismatch at material interfaces.

	Young's modulus, E [GPa]	Longitudinal acoustic velocity, ν_l [m^{-1}s]	Transverse acoustic velocity, ν_t [m^{-1}s]	Longitudinal acoustic impedance, Z_l [Mkg/m^{2}s]	Transverse acoustic impedance, Zt [Mkg/m^{2}s]	Refs.
AlN	308	10 287	6016	33.5	19.6	[22]
*h*BN	865.3	19 600	3850	42.7	8.4	[23]
Graphene	1000	19 900	12 900	45	29.2	[33,34]
Au	70	3428	1122	66.2	21.7	[10]

*h*BN/graphene interface, which acts as an effective acoustic mirror for transverse waves. This mechanism enables strong confinement of acoustic energy within the AlN layer, thereby minimizing radiation losses.

To quantitatively analyze this effect, the reflectivity (R) and transmittivity (T)–representing the ratios of reflected and transmitted energy at the boundary–were calculated for both longitudinal and transverse waves. The acoustic impedances for longitudinal (Z_l) and transverse (Z_t) waves are calculated as follows:

$$Z_l = \nu_l \cdot \rho, \quad Z_t = \nu_t \cdot \rho \tag{7}$$

where ν_l and ν_t are the velocities of longitudinal and transverse waves, respectively, and ρ is the material mass density. The relevant material constants are summarized in **Table 3**.[10,22,23,33,34] The R and T at each interface can be determined by following equations:

$$R_{l,t} = \left| \frac{Z_{l,t}^{(1)} - Z_{l,t}^{(2)}}{Z_{l,t}^{(1)} + Z_{l,t}^{(2)}} \right|^2, \quad T_{l,t} = 1 - R_{l,t} \tag{8}$$

where the superscripts (1), (2) denote the adjacent materials at each interface.

In the multilayer structure of Type-3 LWR, the total reflectivity (R_{total}) and transmittivity (T_{total}) were calculated as follows:

$$R_{total} = R_{AlN/hBN} + \left(T_{AlN/hBN} \cdot R_{hBN/Graphene} \cdot T_{hBN/AlN} \right) \tag{9}$$

$$T_{total} = T_{AlN/hBN} \cdot T_{hBN/Graphene} \tag{10}$$

The calculation results, summarized in **Table 4**, reveal that

Table 4. Reflectivity (R) and transmittivity (T) for longitudinal and transverse waves at the each interface of Type-2 and Type-3 LWR structures.

Structure	Layer stack	Wave type	Reflectivity [R]	Transmittivity [T]
Type-2 LWR	AlN/graphene	Longitudinal	2.15%	97.85%
		Transverse	3.87%	96.13%
Type-3 LWR	AlN/*h*BN (Interface)	Longitudinal	2.2%	97.8%
		Transverse	16%	84%
	*h*BN/graphene (Interface)	Longitudinal	16.22%	83.78%
		Transverse	30.6%	69.4%
	AlN/hBN/graphene (Total)	Longitudinal	1.53%	98.47%
		Transverse	37.59%	58.3%

for longitudinal waves, both Type-2 and Type-3 LWRs show well-matched acoustic impedances and high total transmittivity (Type-2 LWR: 97.85%, Type-3 LWR: 98.47%), enabling efficient energy transfer across interfaces. This is attributed to the Z_l of *h*BN, which lies between the values of AlN and graphene and can effectively bridge the impedance gap between AlN and graphene.

In contrast, for the transverse waves, the total reflectivity of the Type-3 LWR shows a remarkable increase in reflectivity—≈10 times higher (37.59%) than that of the Type-2 LWR (3.87%)—due to the exceptionally low Z_t of *h*BN. The AlN/*h*BN and *h*BN/graphene interfaces in Type-3 LWR show individual reflectivity of 16% and 30.6%, respectively. This sequential impedance mismatch induces multiple internal reflections at each interface, resulting in strong confinement of acoustic energy within the AlN layer and a substantial enhancement in the Q-factor, thereby contributing to the acoustic mirror function provided by the *h*BN/graphene heterostructure. This acoustic mirror effect is further supported by the displacement field distributions shown in Figure 4e, which demonstrate strong energy confinement and reduced leakage into the substrate. Furthermore, if multilayer *h*BN or graphene replaces the monolayer, multiple internal reflections at each interface further enhance the energy confinement. However, multilayer *h*BN's high anisotropy decreases phase velocity and f_r, increasing fabrication difficulty (e.g., high-crystallinity) and interlayer scattering losses.[23]

Beyond its role in acoustic wave confinement, *h*BN/graphene heterostructure also offers several additional benefits. The atomically smooth and inert surface of *h*BN, combined with its similar lattice constant with graphene (1.7% mismatch), provides an ideal substrate for high-quality graphene electronics. This integration reduces defect-induced scattering, supports high carrier mobility, and provides outstanding chemical inertness and environmental stability to the device, resulting in enhanced long-term reliability.[35–37] The virtually massless nature of both *h*BN and graphene minimizes their impact on the cavity structure, potentially mitigating bending effects and improving device reliability. Furthermore, wafer-scale uniformity of monolayer *h*BN/graphene heterostructures can be achieved by direct, sequential chemical vapor deposition (CVD) growth, enabling the scalable fabrication of ultralow-volume acoustic wave devices.[38–40] To enable practical applications, future developments are needed to ensure compatibility of the 2D heterostructure platform with standard CMOS integration processes.[12]
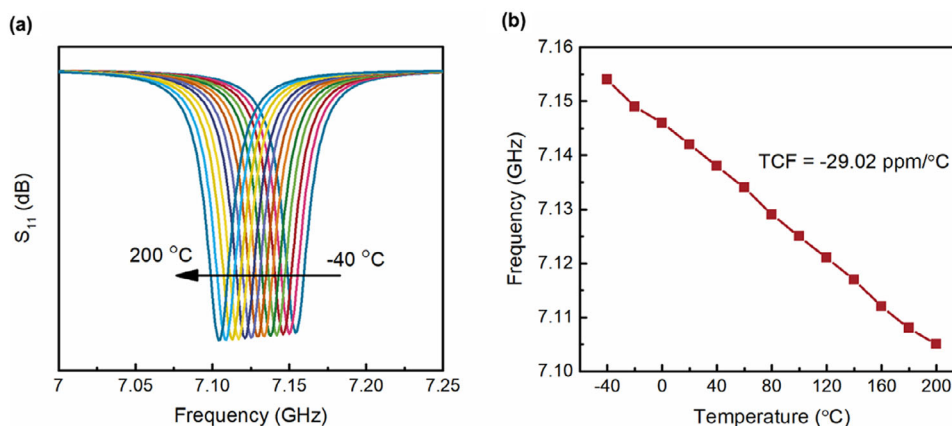
**ADVANCED
SCIENCE NEWS**

www.advancedsciencenews.com

**ADVANCED
MATERIALS
INTERFACES**
Open Access

www.advmatinterfaces.de

Figure 5. Temperature stability analysis of the Type-3 LWR. a) S_{11} at various temperatures (-40 to $200\,°C$), showing a gradual shift in f_r with increasing temperature. b) Linear dependence of f_r on temperature, with a TCF of -29.02 ppm/$°C$, demonstrating the remarkable thermal stability of the Type-3 LWR.

3.2.3. Temperature Stability Analysis

Temperature stability is a crucial factor for ensuring the reliable operation of acoustic wave resonators in practical RF applications. The Type-3 LWR, which incorporates an hBN/graphene heterostructure, demonstrates remarkable thermal stability as evidenced by the temperature dependence of the S0 mode f_r at $h_{AlN}/\lambda = 0.4$, where the FoM is maximized (**Figure 5a**).

Most materials, including AlN and hBN, have negative TCEs, resulting in a decrease in f_r as temperature rises.[41] However, the unique combination of materials in Type-3 LWR offers a compensating thermal expansion effect that can offset f_r decrease. Specifically, AlN possesses a positive thermal expansion coefficient (α), while both hBN and graphene have negative α, as summarized in Table 2. As temperature rises, AlN expands, whereas the hBN/graphene heterostructure contracts. This opposing behavior effectively reduces the net thermal strain within the device, thereby achieving a remarkable TCF and enhancing the thermal stability of the resonator.

As illustrated in Figure 5b, the Type-3 LWR achieves a -29.02 ppm/$°C$, displaying a significant improvement compared to conventional AlN-based LWRs; this value lies within the experimental range of previous study of graphene-AlN resonators, indicating good agreement.[14] This TCF value is even comparable to the devices that employing a SiO_2 temperature compensation layer, a common approach in many studies aiming to achieve a small TCF.[42,43] Notably, the Type-3 LWR achieves this small TCF without the drawbacks associated with the SiO_2 layers, such as reduced f_r due to low acoustic velocity of the SiO_2 and potential degradation caused by additional acoustic losses and interface scattering.

The hBN layer in the heterostructure further acts as a buffer between AlN and graphene. Its intermediate α enables a gradual transition between the expanding AlN and contracting graphene layer, thereby mitigating interfacial stress and enhancing device reliability. It should be noted that the use of multilayer hBN and graphene may not yield the same degree of TCF improvement, as weak van der Waals forces between the layers can result in large out-of-plane thermal expansion (α_{33}).[28,44,45]

In addition to its intrinsic thermal stability, the monolayer hBN/graphene heterostructure offers advantages for device reliability under thermal stress. The high thermal conductivity of the hBN/graphene heterostructure (1072 W/mK) ensures efficient heat dissipation and a uniform temperature distribution across the device, mitigating localized Joule heating that intensifies resistance-related degradation.[24] This property is particularly beneficial in high-frequency applications, where conventional FEs such as Pt or Mo require IDT finger widths to be scaled down to the tens of nanometers range to achieve 6G-band operation. Such extreme scaling increases resistance, leading to power dissipation, thermal stress, and accelerated device degradation. In contrast, the use of graphene as an FE allows for sufficiently large IDT finger widths even at high frequencies, thereby reducing resistance and minimizing degradation mechanisms to further support stable device operation.

4. Conclusion

This study investigates three AlN-based FE-LWRs: Type-1 (IDT/AlN/Pt FE), Type-2 (IDT/AlN/graphene FE), and Type-3 (IDT/AlN/hBN/graphene FE). The research demonstrates that using graphene as a FE significantly improves the f_r (>7 GHz) and k^2 (3.72%) compared to conventional Pt FE. This improvement is attributed to graphene's high Young's modulus, virtually massless nature, and high electrical conductivity.

The integration of the hBN interlayer, forming 2D van der Waals hBN/graphene heterostructure, further enhances RF performances, particularly in terms of Q-factor. This heterostructure acts as an acoustic mirror, effectively reflecting and isolating acoustic energy within the AlN layer due to acoustic impedance mismatch along the transverse direction.

Moreover, the Type-3 LWR demonstrates outstanding temperature stability with a TCF of -29.02 ppm/$°C$, achieved through the opposing thermal expansion of AlN and the hBN/graphene heterostructure. The hBN interlayer acts as a buffer, mitigating interfacial stress between the expanding and contracting layers.

Integration of a 2D hBN/graphene heterostructure as an acoustic mirror significantly improves the Q-factor while enhancing

RF performances and temperature stability. The *h*BN/graphene heterostructure platform shows the potential for adaptation to other LWR devices. These improvements are crucial for 6G wireless communication systems operating in the cm-Wave bands, offering a promising path toward high-performance, temperature-stable acoustic wave devices for next-generation RF technologies.

Conflict of Interest

The authors declare no conflict of interest.

Data Availability Statement

The data that support the findings of this study are available from the corresponding author upon reasonable request.

[1] G. Giribaldi, L. Colombo, P. Simeoni, S. Ghosh, M. Rinaldi, G. Piazza, *Nat. Commun.* **2024**, *15*, 304.

[2] K. Yang, Y. Xie, J. Hu, S. Gong, *Chip* **2023**, *2*, 100058.

[3] G. Xu, Y. Nam, S. Lee, A. Tehrani, D. Y. Lee, A. Prasad, C. Tarver, M. Tonnemacher, Upper Mid-Band Spectrum for 6G: Opportunities and Key Enablers, **2025**.

[4] U. Dropmann, The Golden Bands and the future of 6G **2025**.

[5] M. Rinaldi, C. Zuniga, C. Zuo, G. Piazza, *IEEE Trans. Ultrason. Ferroelectr. Freq. Control* **2010**, *57*, 38.

[6] C. M. Lin, Y. Y. Chen, V. V. Felmetsger, D. G. Senesky, A. P. Pisano, *Adv. Mater.* **2012**, *24*, 2722.

[7] A. Gao, K. Liu, J. Liang, T. Wu, *Microsyst. Nanoeng.* **2020**, *6*, 74.

[8] V. Yantchev, I. Katardjiev, *J. Micromech. Microeng.* **2013**, *23*, 043001.

[9] J. Bijurström, I. Katardjiev, V. Yantchev, *Appl. Phys. Lett.* **2005**, *86*, 154103.

[10] J. Zou, C. M. Lin, C. S. Lam, A. P. Pisano, *J. Appl. Phys.* **2017**, *121*, 154502.

[11] Z. Wan, H. Liu, Y. Zheng, Y. Ma, K. Liu, X. Zhou, C. Liu, K. Liu, E. Wang, *Adv. Funct. Mater.* **2024**, *34*, 2303519.

[12] B. Xu, P. Zhang, J. Zhu, Z. Liu, A. Eichler, X.-Q. Zheng, J. Lee, A. Dash, S. More, S. Wu, Y. Wang, H. Jia, A. Naik, A. Bachtold, R. Yang, P. X.-L. Feng, Z. Wang, *ACS Nano* **2022**, *16*, 15545.

[13] Z. Qian, F. Liu, Y. Hui, S. Kar, M. Rinaldi, *Nano Lett.* **2015**, *15*, 4599.

[14] Z. Qian, Y. Hui, F. Liu, S. Kang, S. Kar, M. Rinaldi, *Microsyst. Nanoeng.* **2016**, *2*, 16026.

[15] M. Knapp, R. Hoffmann, V. Lebedev, V. Cimalla, O. Ambacher, *Nanotechnology* **2018**, *29*, 105302.

[16] T.-T. Yen, A. P. Pisano, C. T.-C. Nguyen, *Proc. IEEE Int. Conf. Micro Electro Mech. Syst*, IEEE, Taipei, Taiwan, **2013**, 114.

[17] J. Segovia-Fernandez, N.-K. Kuo, G. Piazza, in *IEEE International Ultrasonics Symposium*, **2012**, IEEE, Dresden, Germany, 299.

[18] J. Rodriguez, S. A. Chandorkar, C. A. Watson, G. M. Glaze, C. H. Ahn, E. J. Ng, Y. Yang, T. W. Kenny, *Sci. Rep.* **2019**, *9*, 2244.

[19] S. Shao, Z. Luo, T. Wu, *IEEE Electron Device Lett.* **2021**, *42*, 1378.

[20] R. A. Barton, B. Ilic, A. M. van der Zande, W. S. Whitney, P. L. McEuen, J. M. Parpia, H. G. Craighead, *Nano Lett.* **2011**, *11*, 1232.

[21] Z. Su, L. Ye, *Identification of Damage Using Lamb Waves*, Springer, London, UK **2009**.

[22] J. Bijurström, G. Wingqvist, V. Yantchev, I. Katardjiev, *J. Micromech. Microeng.* **2007**, *17*, 651.

[23] S. H. Yoon, C.-K. Baek, B. D. Kong, *Sci. Rep.* **2022**, *12*, 20475.

[24] S. Karak, S. Paul, D. Negi, B. Poojitha, S. K. Srivastav, A. Das, S. Saha, *ACS Appl. Nano Mater.* **2021**, *4*, 1951.

[25] J. I.-J. Wang, M. A. Yamoah, Q. Li, A. H. Karamlou, T. Kinh, B. Kannan, J. Braumüller, D. Kim, A. J. Melville, S. E. Muschinske, B. M. Niedzielski, K. Serniak, Y. Sung, R. Winik, J. L. Yoder, M. E. Schwartz, K. Watanabe, T. Taniguchi, T. P. Orlando, S. Gustavsson, P. Jarillo-Herrero, W. D. Oliver, *Nat. Mater.* **2022**, *21*, 398.

[26] T.-H. Hsu, Z.-Q. Lee, G.-L. Wu, C.-C. Yeh, C.-H. Tsai, M.-H. Li, *IEEE Trans. Ultrason. Ferroelectr. Freq. Control* **2024**, *71*, 1324.

[27] L. He, H. Wang, L. Chen, X. Wang, H. Xie, C. Jiang, C. Li, K. Elibol, J. Meyer, K. Watanabe, T. Taniguchi, Z. Wu, W. Wang, Z. Ni, X. Miao, C. Zhang, D. Zhang, H. Wang, X. Xie, *Nat. Commun.* **2019**, *10*, 2815.

[28] G. A. Slack, S. F. Bartram, *J. Appl. Phys.* **1975**, *46*, 89.

[29] B. Yates, M. J. Overy, O. Pirgon, *Pilos. Mag* **1975**, *32*, 847.

[30] D. Yoon, Y.-W. Son, H. Cheong, *Nano Lett.* **2011**, *11*, 3227.

[31] J.-H. Jou, C.-N. Liao, K.-W. Jou, *Thin Solid Films* **1994**, *238*, 70.

[32] Y. Yan, L. D. Geng, H. Liu, H. Leng, X. Li, Y. U. Wang, S. Priya, *Nat. Commun.* **2022**, *13*, 3565.

[33] C. Lee, X. Wei, J. W. Kysar, J. Hone, *Science* **2008**, *321*, 385.

[34] X. Cong, Q.-Q. Li, X. Zhang, M.-L. Lin, J.-B. Wu, X.-L. Liu, P. Venezuela, P.-H. Tan, *Carbon* **2019**, *149*, 19.

[35] C. Dean, A. F. Young, I. Meric, C. Lee, L. Wang, S. Sorgenfrei, K. Watanabe, T. Taniguchi, P. Kim, K. L. Shepard, J. Hone, *Nat. Nanotechnol.* **2010**, *5*, 722.

[36] J. Wang, F. Ma, M. Sun, *RSC Adv.* **2017**, *7*, 16801.

[37] Q. Li, M. Liu, Y. Zhang, Z. Liu, *Small* **2016**, *12*, 32.

[38] M. Wang, S. K. Jang, W.-J. Jang, M. Kim, S.-Y. Park, S.-W. Kim, S.-J. Kahng, J.-Y. Choi, R. S. Ruoff, Y. J. Song, S. Lee, *Adv. Mater.* **2013**, *25*, 2746.

[39] K. Kang, K.-H. Lee, Y. Han, H. Gao, S. Xie, D. A. Muller, J. Park, *Nature* **2017**, *550*, 229.

[40] K. H. Lee, H.-J. Shin, J. Lee, I.-Y. Lee, G.-H. Kim, J.-Y. Choi, S.-W. Kim, *Nano Lett.* **2012**, *12*, 714.

[41] T. Han, Y. Luo, C. Wang, *J. Phys. D: Appl. Phys.* **2014**, *47*, 025303.

[42] J. Zou, C.-M. Lin, Y.-Y. Chen, A. P. Pisano, *J. Appl. Phys.* **2014**, *115*, 094510.

[43] G. Wingqvist, L. Arapan, V. Yantchev, I. Katardjiev, *J. Micromech. Microeng.* **2009**, *19*, 035018.

[44] H. O. Pierson, *Handbook of Carbon, Graphite, Diamonds and Fullerenes: Processing, Properties and Applications*, Noyes Publications, Park Ridge, NJ **1993**.

[45] X. Y. Fang, X. X. Yu, H. M. Zheng, H. B. Jin, L. Wang, M. S. Cao, *Phys. Lett. A* **2015**, *379*, 2245.